Advances in Water Resources 113 (2018) 141–154

Contents lists available at ScienceDirect

Advances in Water Resources

journal homepage: www.elsevier.com/locate/advwatres

Shear and shearless Lagrangian structures in compound channels

Enrile F.*, Besio G., Stocchino A.

DICCA, Dipartimento di Ingegneria Civile, Chimica e Ambientale, Università degli Studi di Genova, Italia

ARTICLE INFO

Keywords:
Shear Lagrangian Structure
Shearless Lagrangian Structure
Ridges
Trenches
FTLE
Shearlines
River dynamics

ABSTRACT

Transport processes in a physical model of a natural stream with a composite cross-section (compound channel) are investigated by means of a Lagrangian analysis based on nonlinear dynamical system theory. Two-dimensional free surface Eulerian experimental velocity fields of a uniform flow in a compound channel form the basis for the identification of the so-called Lagrangian Coherent Structures. Lagrangian structures are recognized as the key features that govern particle trajectories. We seek for two particular class of Lagrangian structures: Shear and shearless structures. The former are generated whenever the shear dominates the flow whereas the latter behave as jet-cores. These two type of structures are detected as ridges and trenches of the Finite-Time Lyapunov Exponents fields, respectively. Besides, shearlines computed applying the geodesic theory of transport barriers mark Shear Lagrangian Coherent Structures. So far, the detection of these structures in real experimental flows has not been deeply investigated. Indeed, the present results obtained in a wide range of the controlling parameters clearly show a different behaviour depending on the shallowness of the flow. Shear and Shearless Lagrangian Structures detected from laboratory experiments clearly appear as the flow develops in shallow conditions. The presence of these Lagrangian Structures tends to fade in deep flow conditions.

1. Introduction

Natural rivers and, quite often, artificial channels are characterized by cross-sections composed by a deeper main channel and shallower floodplains. For this reason they are usually referred as “compound channels”. Flows of these streams are defined as predominantly horizontal since their horizontal dimensions greatly exceed the vertical one (Jirka, 2001).

The analysis of mixing processes in natural streams is not a simple task as flow dynamics is strongly affected by channel irregularities. Flow velocity in the floodplains is lower than the one of the main channel, due to the water shallowness and to bed roughness typically higher than the main channel. As a result of the velocity gradient, shear occurs at the interface between the main channel and the floodplains. The presence of various Eulerian flow patterns most of which are characterized by large-scale vortical structures with vertical axes, i.e. macro-vortices, is well-known (Socolofksy and Jirka, 2004; Stocchino et al., 2011; Stocchino and Brocchini, 2010). The generation of these vortical structures can be described by two main approaches (Rowiński and Radecki-Pawlik, 2015): either as a shear instability at the junction of two streams (van Prooijen et al., 2005) or as an outcome of differential energy dissipation of shallow-water currents interacting with submerged obstacles (Soldini et al., 2004). The former approach casts an analogy between the transitional region of the compound channel and a free mixing layer. The latter identifies the driving mechanism for the generation and sustainment of the Eulerian macro-vortices in the vorticity generation owing to the depth jump across the cross-section. Stocchino and Brocchini (2010) showed that the shear layer thickness remains constant in compound channels. Such a condition is a peculiar consequence of the topographic forcing, i.e. the depth jump, generating the Eulerian macro-vortices. On the contrary, the shear layer generated by the junction of two streams on an even bottom tends to grow linearly. In order to clarify strengths and shortcomings of both, a detailed comparison between the approaches pursued by van Prooijen et al. (2005) and Soldini et al. (2004) should be carried out and the outcome of the numerical simulations compared. However, the issues raised by these two different approaches are not considered in the present work. Indeed, we aim to analyse experimental surface velocity fields under a Lagrangian perspective disregarding the Eulerian approach. Note that it is well-known that Eulerian and Lagrangian patterns do not always correspond (Haller, 2015).

An experimental investigation on the mixing processes, in terms of Lagrangian statistics of single and multiple particles, was presented by Stocchino et al. (2011). However, the role of flow inhomogeneity was disregarded in that study. This aspect is the main subject of the present work, where we aim to detect coherent patterns from Lagrangian measures in order to seek structures that characterise the compound channel. Key structures are located at the transition from the main

* Corresponding author.
E-mail address: francesco.enrile@edu.unige.it (E. F.).

https://doi.org/10.1016/j.advwatres.2018.01.006
Received 1 August 2017; Received in revised form 5 January 2018; Accepted 6 January 2018
Available online 06 February 2018
0309-1708/

channel to the lateral channels (floodplains) and approximately along the axis of the main channel. Therefore, we focus on Lagrangian structures that shape trajectory patterns.

The present analysis mainly relies on the computations of the Finite Time Lyapunov Exponents (FTLE) fields along with related trenches (Beron-Vera et al., 2010) and ridges (Shadden et al., 2005), as a first diagnostic tool. However, FTLE trenches and ridges are not always a signature of the presence of material lines. Despite such a shortcoming, they are still a valuable tool to understand the dynamics of the flow. In particular, ridges are able to reveal the regions of motion that are kinematically the most active (Allshouse and Peacock, 2015a). We then manage to isolate two types of heuristic structures that are mostly disregarded in previous studies: Jet-Cores (JC), i.e. shearless structures, and Shear Lagrangian Structures (SLS), respectively. JC were studied by Beron-Vera et al. (2010) and Farazmand et al. (2014). In the present work we apply the methodology detailed in the former study based on FTLE trenches. Besides, we characterize the behaviour of heuristic JC resulting from FTLE trenches by applying the methodology described by Allshouse and Peacock (2015b). The same method is also applied to ridges of FTLE fields that mark heuristic SLS. Such a conclusion is proven by testing heuristic SLS against their shear properties.

A further characterization of shear is carried out upon the rigorous definitions of Lagrangian Coherent Structures (LCS) (Haller, 2011; Haller and Beron-Vera, 2012). Among the general family of LCS, SLS are features dominated by a bulk shear typical of parallel flows. Herein, SLS are detected in order to mark the fundamental geometry of shear patterns. Note that SLS and JC are usually defined and studied on the basis of analytical velocity fields, whereas the main goal of the present study is to deeply investigate realistic flow conditions in a laboratory model of a typical river configuration. Heuristic SLS calculated as FTLE ridges and rigorous SLS calculated from the geodesic theory of transport barriers are compared and a nice agreement is found.

Summing up, experimental data of time-dependent, two-dimensional Eulerian velocity fields (Stocchino et al., 2011; Stocchino and Brocchini, 2010) are employed to calculate numerical trajectories upon which JC and SLS are estimated against their shear properties. Rigorous SLS are also calculated as shearlines that minimize their geodesic deviation.

The paper proceeds with Section 2 devoted to the definition and formulation of the LCS identification techniques. Then, in Section 3 we describe the velocity fields employed and we asses their two-dimensionality. Section 4 describes in details the LCS that can be detected in shallow, intermediate, and deep flow conditions. Finally, Section 5 is devoted to the conclusions and closes the paper.

2. Theoretical background

A fluid is usually studied applying the well-known results of continuum mechanics and we follow this approach. A fluid body $\mathscr{B}$ is made of elements called particles ξ. In order to describe the position of these particles we establish a one-to-one correspondence between the particles and the coordinates of a reference system, i.e. a triple of real numbers. We introduce Lagrangian coordinates $\boldsymbol{\xi} = (\xi^1, \xi^2, \xi^3)$ as a material coordinate system that label fluid particles. Since any two systems of coordinates are related by a continuously differentiable transformation we can introduce Eulerian coordinates as

$$\boldsymbol{x} = \boldsymbol{\Phi}(t; t_0, \boldsymbol{\xi}) \tag{1}$$

where $\boldsymbol{\Phi}$ is the flow map. The Eulerian coordinates denote the position of a point fixed in what can be called the laboratory frame (Thiffeault and Boozer, 2001). The transformation showed in equation (1) can be inverted in the neighbour of a point provided that the Jacobian exists and does not vanish (Aris, 1962).

The study of fluid flows cannot be carried out disregarding velocity fields. Indeed, velocity fields are the core of fluid mechanics and time-dependent velocity fields are generally written as $\boldsymbol{v}(\boldsymbol{x}, t)$. The trajectory of particles are curves solutions of

$$\frac{d\boldsymbol{x}}{dt} = \boldsymbol{v}(\boldsymbol{x}, t) \tag{2}$$

with initial conditions $\boldsymbol{x}(t_0, \boldsymbol{\xi}) = \boldsymbol{\xi}$.

We can regard Eq. (2) as a set of ordinary differential equations and evaluate on a finite time interval $T = (t_1 - t_0)$ the distance that two initial close particles can experience. Therefore, if we consider as initial conditions $\boldsymbol{\xi}_0$ and $\boldsymbol{\xi}_0 + \boldsymbol{\epsilon}$ we can evaluate the final distance between the two particles applying a linearisation (Allshouse and Peacock, 2015b):

$$\delta\boldsymbol{x}(t_1) = \boldsymbol{\Phi}(t_1; t_0, \boldsymbol{\xi}_0) - \boldsymbol{\Phi}(t_1; t_0, \boldsymbol{\xi}_0 + \boldsymbol{\epsilon}) \approx \nabla\boldsymbol{\Phi}(t_1; t_0, \boldsymbol{\xi}_0)\boldsymbol{\epsilon} \tag{3}$$

where $\nabla\boldsymbol{\Phi}(t_1; t_0, \boldsymbol{\xi}_0)$ is called the flow map gradient and it is a tensor represented by a matrix the entries of which are $\nabla\Phi^i_j = \partial x^i/\partial\xi^j$. We impose two restrictions on $\nabla\boldsymbol{\Phi}$. Firstly, an infinitesimal material element $d\boldsymbol{x}$ must not split along its evolution and coalescence of two material elements is not allowed. This is the physical interpretation of the condition on the Jacobian of Eq. (1). The second restriction imposes that the deformation must preserve orientation, i.e. three right-handed material elements $d\boldsymbol{x}$, $d\boldsymbol{y}$ and $d\boldsymbol{z}$ satisfying $d\boldsymbol{x}\wedge d\boldsymbol{y}\cdot d\boldsymbol{z} > 0$ are transformed into three material elements satisfying $d\boldsymbol{x}(t) \wedge d\boldsymbol{y}(t)\cdot d\boldsymbol{z}(t) = (\nabla\boldsymbol{\Phi} d\boldsymbol{x}) \wedge (\nabla\boldsymbol{\Phi} d\boldsymbol{y})\cdot(\nabla\boldsymbol{\Phi} d\boldsymbol{z}) = \det(\nabla\boldsymbol{\Phi}) d\boldsymbol{x} \wedge d\boldsymbol{y}\cdot d\boldsymbol{z} > 0$. By writing $\nabla\boldsymbol{\Phi} d\boldsymbol{x}$ we denote the product between the matrix $\nabla\boldsymbol{\Phi}$ and the vector $d\boldsymbol{x}$, i.e. a contraction that results in a vector. Scalar product between vectors is indicated as $(\cdot)$. The second restriction implies that the Jacobian of Eq. (1) must satisfy the following condition:

$$J = \det(\nabla\boldsymbol{\Phi}) > 0 \tag{4}$$

The magnitude of the final distance can be evaluated as (Shadden et al., 2005):

$$\begin{aligned}|\delta\boldsymbol{x}(t_1)| &= \sqrt{\delta\boldsymbol{x}(t_1)\cdot\delta\boldsymbol{x}(t_1)} = \sqrt{[\nabla\boldsymbol{\Phi}\delta\boldsymbol{x}(t_0)]\cdot[\nabla\boldsymbol{\Phi}\delta\boldsymbol{x}(t_0)]} = \\ &= \sqrt{\delta\boldsymbol{x}(t_0)\cdot[\boldsymbol{C}\delta\boldsymbol{x}(t_0)]} = \sqrt{\boldsymbol{\epsilon}\cdot(\boldsymbol{C}\boldsymbol{\epsilon})}\end{aligned} \tag{5}$$

where $\boldsymbol{C}$ is the Cauchy-Green tensor defined as $\boldsymbol{C} = (\nabla\boldsymbol{\Phi})^T\nabla\boldsymbol{\Phi}$ where $(\cdot)^T$ denotes the transpose. It is possible to prove that matrix $\boldsymbol{C}$ is positive definite and symmetric. Since we analyse 2D velocity fields, $\boldsymbol{C}$ has two eigenvectors $\boldsymbol{e}_1$ and $\boldsymbol{e}_2$ associated with two eigenvalues $0 < \lambda_1 \le \lambda_2$, respectively.

Maximum stretching occurs when $\delta\boldsymbol{x}(t_0)$ is chosen such that it is aligned with the eigenvector associated with the maximum eigenvalue of $\boldsymbol{C}$, i.e.:

$$\max|\delta\boldsymbol{x}(t_1)| = \sqrt{\lambda_2}\,|\overline{\delta\boldsymbol{x}}(t_0)| \tag{6}$$

where $\overline{(\cdot)}$ indicates alignment with the eigenvector associated with the maximum eigenvalue λ_2 of the Cauchy–Green tensor. Since $\delta\boldsymbol{x}(t_0) = \boldsymbol{\epsilon}$, Eq. (6) can be recast to obtain

$$\max|\delta\boldsymbol{x}(t_1)| = e^{\sigma_{t_0}^{t_1}|T|}|\bar{\boldsymbol{\epsilon}}| \tag{7}$$

where

$$\sigma_{t_0}^{t_1} = \frac{1}{|T|}\log\sqrt{\lambda_2} \tag{8}$$

represents the (maximum) Finite-Time Lyapunov Exponent (FTLE) calculated on a finite integration time T.

The eigenvectors of $\boldsymbol{C}$ define directions of initial separations for which neighbouring particles are converging or diverging. Since we are interested in the most active regions of the fluid flow from a kinematic point of view, we define the FTLE in Eq. (8) as a function of the maximum eigenvalue. Panel a) of Fig. 1 shows the deformation in the neighboured of a point under the action of the flow map. Computation of FTLE can be carried out in forward time, i.e. from t_0 to $t_0 + T$, or in backward time, i.e. from $t_0 + T$ to t_0. Identification and classification of the main features of these scalar fields is the subject of the next paragraphs.

Eckmann and Ruelle (1985) showed how λ_2 tends asymptotically to

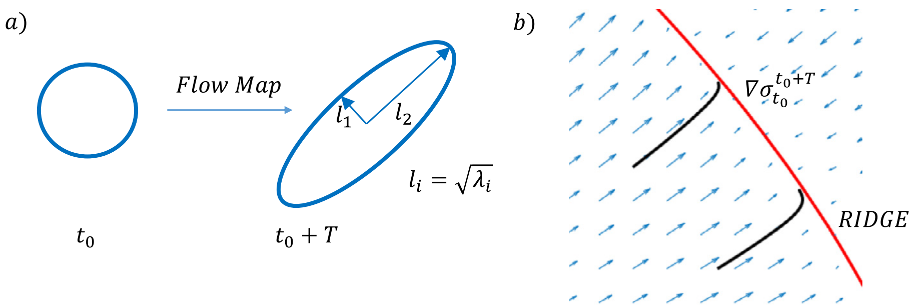

Fig. 1. Panel a) shows the deformation in the neighbourhood of a point under the flow map $\boldsymbol{\Phi}$. A circle of unit radius is deformed as depicted. Panel b) shows the vector field $\nabla\sigma_{t_0}^{t_1}$, a ridge, in red, and two solutions of Eq. (12), in black. (For interpretation of the references to colour in this figure legend, the reader is referred to the web version of this article.)

a single value λ_∞ as time tends to infinity for ergodic systems. The following results are strictly applicable to autonomous systems (Osseledec theorem):

$$\lambda_\infty = \lim_{T\to\infty} \frac{\log(\lambda_2)}{2T} \tag{9}$$

Tang and Boozer (1996) showed that at times $T \gg \frac{1}{\lambda_\infty}$ the averaged FTLE takes the form:

$$\langle\lambda\rangle = \frac{A}{T} + \frac{B}{\sqrt{T}} + \lambda_\infty \tag{10}$$

where A and B are constants. Analogously, the standard deviation behaves as:

$$\sigma_\lambda \propto \sqrt{\frac{1}{T}} \tag{11}$$

The probability density function must behave in agreement with the previous theoretical results, i.e. as the integration time increases the pdf must narrow, converging to a delta function. Abraham and Bowen (2002) showed the consistency of these last theoretical results in an analysis carried out on the basis of surface velocity fields of a region of the East-Australian Current. Lapeyre (2002) found narrowing pdfs as T increases, due to the decrease of the standard deviation, and a shift of the peaks towards smaller values due to the decaying turbulent field in time he analysed.

2.1. Detection and classification of the FTLE features: Ridges and trenches

Lagrangian Coherent Structures have been broadly recognised as the main features that characterise transport in fluid flows. FTLE scalar fields have been largely adopted in order to seek for heuristic Lagrangian Coherent Structures. In particular, ridges have been associated with the concept of stable and unstable manifolds: ridges calculated in forward time are considered as a signature of repelling structures whereas ridges calculated in backward time as attracting structures (Shadden et al., 2005). However, such a representation is undermined by some known issues (Haller and Yuan, 2000). In particular, ridges of FTLE fields can mark heuristic SLS. This applies to the present case: the transition region between the main channel and the floodplains is marked by such features, as discussed in the following.

JC can be detected at the center of the main channel. They mark absence of shear and inhibit cross-channel transport: Such shearless barriers were found to strongly separate the fluid environment preventing exchange between the regions divided by them (Rypina et al., 2007; Samelson, 1992). Such structures were classified as invariant-tori-like LCS that are often present in geophysical flows (Beron-Vera et al., 2010). Since infinite-time Lyapunov exponents of invariant-tori are zero and invariant-tori computed in forward time coincide with invariant-tori computed in backward time, the heuristic identification of JC relies on trenches of FTLE fields that coincide in forward and backward time.

Evaluation of the most influential structures in FTLE fields, i.e. ridges and trenches, is pursued considering the dynamical properties of these features (Green et al., 2007; Mathur et al., 2007). Ridges behave as attractors of trajectories solution of the dynamical system

$$\frac{d\boldsymbol{x}}{ds} = \nabla\sigma_{t_0}^{t_0\pm T}(\boldsymbol{x}) \tag{12}$$

where s is the arclength along the gradient lines of $\sigma_{t_0}^{t_0\pm T}(\boldsymbol{x})$ and the right-hand side represents the spatial gradient of FTLE scalar fields. This property is at the base of the extraction algorithm proposed by Mathur et al. (2007) and here adopted. The reliability of such a procedure was strengthen by Peikert et al. (2013). Panel b) of Fig. 1 shows the behaviour of ridges as attractors of trajectories solution of Eq. (12). The detection of trenches is analogue: the computations are carried out considering $\frac{dx}{ds} = -\nabla\sigma_{t_0}^{t_0\pm T}(\boldsymbol{x})$. Since the methodology is the same, in the following we refer only to ridges.

Once the ridges are detected, a hermite interpolation is adopted (Rovenski, 2010) in order to locate (first attempt) ridges made of points equally spaced between them. The advantage of Hermite cubic interpolation is twofold. Tangent vectors of the points that form the curve can be chosen and monotony property of the function (curve) that is interpolated is generally preserved. Given points P_1 and P_2 and nonzero tangent vectors Q_1 and Q_2 the cubic Hermite curve $r(s)$ is defined as

$$r(s) = (1 - 3s^2 + 2s^3)P_1 + s^2(3 - 2s)P_2 + s(s-1)^2Q_1 + s^2(s-1)Q_2 \tag{13}$$

where $0 \le s \le 1$. However, the precision of the computed ridges is insufficient to allow for an accurate advection of these structures. Therefore, the procedure described by Allshouse and Peacock (2015b) is applied in order to refine the ridges. Following the cited approach, points belonging to a ridge are detected with a relative precision of order 10^{-7} and their advection can be reliably computed. The refinement process is schematically depicted in Fig. 2 and can be summarized as follows. An initial ridge (depicted in red in Fig. 2, i.e. the curve interpolated with the Hermite polynomial) is better approximated placing a number of test points at incremental distances δ at either sides of the ridge along the normal direction. FTLE values for all these points normal to the initial ridge are then evaluated and the point with the maximum FTLE value is taken as the refined position of the ridge (green points in Fig. 2). In case of trenches, the revised position is chosen as the corresponding minimum FTLE value.

This process is carried out recursively until a prescribed accuracy is reached. Once the final (refined) ridge is calculated, it is possible to define a tangential unit vector $\boldsymbol{\tau_0}$ to the ridge at time t_0 and a normal unit vector $\boldsymbol{n_0}$, evaluated with Frenet–Serret formulas. By applying the flow map gradient, we can evaluate the advected tangential vector $\nabla\boldsymbol{\Phi}\boldsymbol{\tau_0}$ and the advected normal vector $\nabla\boldsymbol{\Phi}\boldsymbol{n_0}$.

In order to characterize the behaviour of ridges it is possible to evaluate the quantities described by Allshouse and Peacock (2015b). The magnitudes of the advected normal and tangential vectors, n_l and e_l, show stretching and contraction that occur to particles initially aligned along the ridge and initially perpendicular to the ridge, respectively, and can be written as:

$$n_l = \log|\nabla\boldsymbol{\Phi}\boldsymbol{n_0}| \tag{14}$$

$$e_l = \log|\nabla\boldsymbol{\Phi}\boldsymbol{\tau_0}| \tag{15}$$

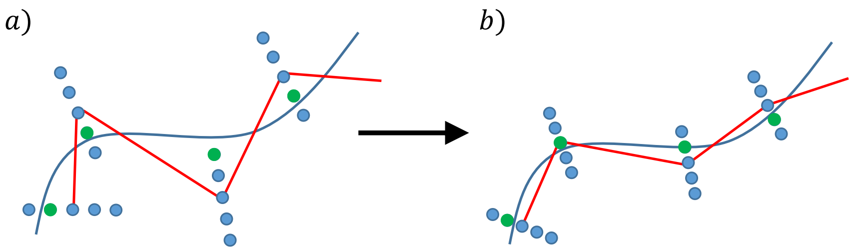

Fig. 2. The refinement process adopted from Allshouse and Peacock (2015b). The true ridge is depicted in blue. Initial guess ridge is depicted in red on the left. New maximum FTLE positions are circled in green. After recursively applying the refinement process, as shown on the right, the ridge is better approximated. (For interpretation of the references to colour in this figure legend, the reader is referred to the web version of this article.)

Similarly, it is possible to compute the hyperbolic repulsion ρ_l and the Lagrangian shear σ_l in order to characterize how the unit normal vector $\boldsymbol{n_0}$ deforms, as:

$$\rho_l \quad = \log|[\boldsymbol{n_t}\cdot(\nabla\boldsymbol{\Phi}\boldsymbol{n_0})]| \tag{16}$$

$$\sigma_l \quad = \log|[\boldsymbol{\tau_t}\cdot(\nabla\boldsymbol{\Phi}\boldsymbol{n_0})]| \tag{17}$$

where $\boldsymbol{n_t}$ and $\boldsymbol{\tau_t}$ are unit normal and tangential vectors to the advected ridge. Fig. 3 shows a pictorial representation of such quantities. Eqs. (14)–(17) adopt a logarithmic scaling in order emphasize stretching. A precise detection of the ridges is mandatory for a reliable computation of the quantities expressed by Eqs. (14)–(17), in particular when the flow map gradient is applied to $\boldsymbol{\tau_0}$. Trenches of FTLE fields are characterized adopting the same measures. The predominant shear character of ridges is confirmed if σ_l is greater than ρ_l along the majority of their length. On the contrary, JC must present very small σ_l and vanishing ρ_l along the majority of their length.

2.2. Shear Lagrangian coherent structures

Recent developments in the field of Lagrangian Structures cleared that not all FTLE ridges are material lines. Haller and Beron-Vera (2012) developed a consistent theory in order do detect material lines that act as transport barriers. Of particular interest are material lines that attract or repel nearby fluid over a finite time interval. The normal repulsion rate introduced in the previous section evaluates such a condition (logarithmic scaling is not essential in the definition). Necessary and sufficient criteria for the existence of repelling and attracting LCS over a finite time interval are described in terms of eigenvalues and eigenvectors of the Cauchy–Green tensor. Adopting a variational argument, Haller and Beron-Vera (2012) showed that a curve is a hyperbolic transport barrier whether it is a trajectory of the autonomous differential equation:

$$\boldsymbol{r}' = \boldsymbol{e}_1 \tag{18}$$

Such trajectories are defined strainlines after Haller and Beron-Vera (2012). Considering a generic point P, the least-stretching geodesic at P under the Cauchy–Green tensor is the geodesic starting from P with a unit tangent vector expressed by Eq. (18).

In the framework of this work, the predominant features of the flow are characterised by shear. The material lines, shear LCS, that maximize Lagrangian shear $\sigma = \tau_t\cdot(\nabla\boldsymbol{\Phi}\boldsymbol{n_0})$ are curves everywhere tangent to the shear vector field $\boldsymbol{\eta}_{\pm}$ (Hadjighasem et al., 2013; Haller and Beron-Vera, 2012) defined as:

$$\boldsymbol{\eta}_{\pm} = \sqrt{\frac{\sqrt{\lambda_2}}{\sqrt{\lambda_1}+\sqrt{\lambda_2}}}\,\boldsymbol{e}_1 \pm \sqrt{\frac{\sqrt{\lambda_1}}{\sqrt{\lambda_1}+\sqrt{\lambda_2}}}\,\boldsymbol{e}_2 \tag{19}$$

Open curves tangent to the shear vector field of Eq. (19) are shear LCS, i.e. a shear transport barrier is a trajectory of the autonomous differential equation:

$$\boldsymbol{r}' = \boldsymbol{\eta}_{\pm} \tag{20}$$

Such trajectories are defined shearlines after Haller and Beron-Vera (2012). Positive Lagrangian shear signals clockwise deformation while negative Lagrangian shear signals counterclockwise deformation in the local coordinate frame $(\boldsymbol{e}_1, \boldsymbol{e}_2)$. The most prominent shear LCS are shearlines that minimize the geodesic shear deviation (Hadjighasem et al., 2013; Haller and Beron-Vera, 2012) along their length. The pointwise closeness of shear LCS to least-stretching geodesics can be computed in terms of invariants of the Cauchy-Green tensor. The geodesic deviation evaluates the difference of tangents plus the difference of curvatures of a shear LCS from the least-stretching geodesic of the Cauchy-Green tensor. Haller and Beron-Vera (2012) provide an explicit formula in order to evaluate the geodesic deviation, which reads:

$$\begin{aligned} d_g^{\eta_\pm} = & \frac{\sqrt{1+\lambda_2}-\sqrt{\lambda_2}}{\sqrt{1+\lambda_2}} + \frac{\nabla\lambda_2\cdot\boldsymbol{e}_1}{2\lambda_2\sqrt{1+\lambda_2}} \\ & \mp \frac{\langle\nabla\lambda_2, \boldsymbol{e}_2\rangle\left(\sqrt{1+\lambda_2}^{\,3}-\sqrt{\lambda_2}^{\,5}\right)}{2\lambda_2^3\sqrt{1+\lambda_2}^{\,3}} \\ & \mp \frac{\kappa_1\left[\sqrt{\lambda_2}^{\,5}+(1-\lambda_2^2)\sqrt{1+\lambda_2}\right]}{\lambda_2^2\sqrt{1+\lambda_2}} + \frac{\kappa_2}{\sqrt{1+\lambda_2}} \end{aligned} \tag{21}$$

with $\boldsymbol{e}_2$ denoting the eigenvector associated with λ_2, κ_1 the curvature of the strainline and κ_2 the curvature of $\boldsymbol{e}_2$ vector field. The predominant shear LCS is chosen as the shearline whose average geodesic deviation

$$\mathrm{avg}(d_g^{\eta_\pm}) = \frac{\int d_g^{\eta_\pm}|\boldsymbol{r}'|ds}{\int|\boldsymbol{r}'|ds} \tag{22}$$

is the least among all. Computations of FTLE fields and shear LCS are carried out following Onu et al. (2015) and Farazmand and Haller (2012). A MATLAB toolbox was made publicly available by these authors and it has been here exploited.

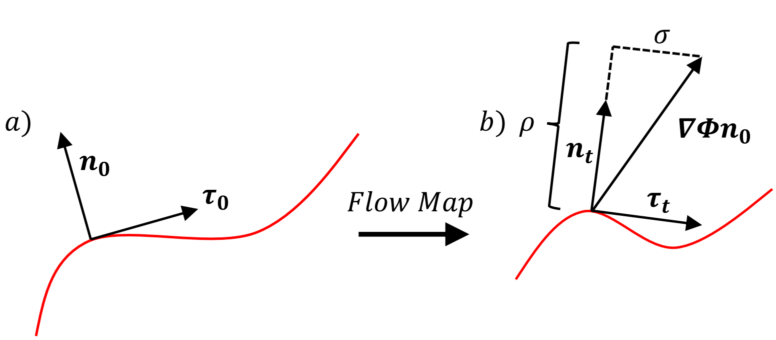

Fig. 3. Pictorial representation of unit normal and tangential vectors and of hyperbolic repulsion and Lagrangian shear. Note that logarithmic scaling is not applied to this picture.

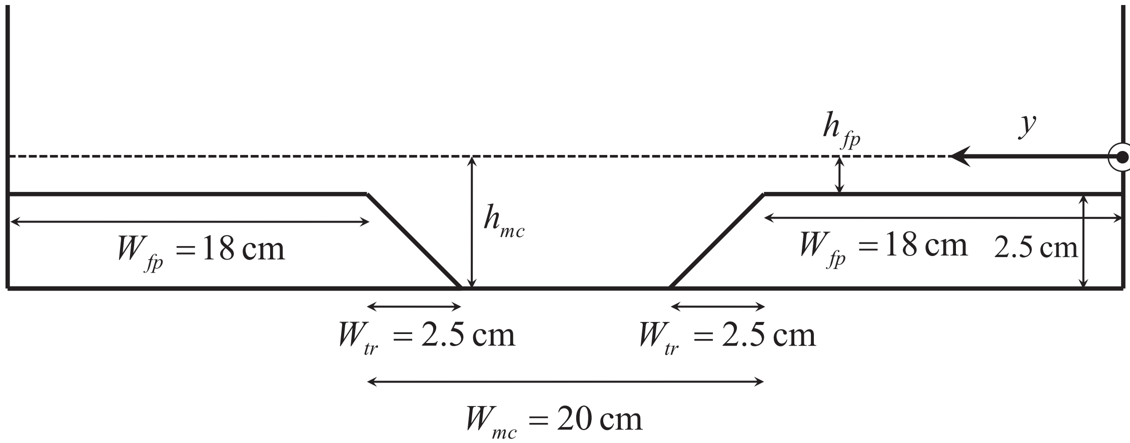

Fig. 4. Sketch of the cross section of the flume.

3. Experimental flow field

The present analysis is based on the experimental measurements of the free-surface Eulerian velocity fields described in Stocchino and Brocchini (2010) and Stocchino et al. (2011). Herein, we briefly recall the main characteristics of the apparatus and of the measuring system. The flume was 20 m long, 60 cm wide and the trapezoidal cross-section was composed by a central main channel (W_{mc}= 20 cm), two lateral flat floodplains (W_{fp}= 18 cm) and a transition region (W_{tr}= 2.5 cm). Fig. 4 shows the cross section of the flume.

Velocity measurements have been performed by means of a two-dimensional Particle Image Velocimetry system on a field of view of (1.2 × 0.6) m^2. The acquisition rate was between 100 Hz and 250 Hz, depending on the flow velocity. Each acquisition was made of a number of frames between 2000 and 4000. Several series of experiments have been carried out spanning a quite large range of values of the main physical parameters. In Table 1 we summarize the experimental conditions, providing the values of the ratio between the main channel water depth (h_{mc}) and that of the floodplains (h_{fp}), $r_h = h_{mc}/h_{fp}$, and the Froude number, $Fr = U_m/\sqrt{gR}$, where R is the hydraulic radius, g is gravity and U_m is the peak velocity in the main channel. Moreover, S represents the longitudinal bed slope.

We keep the same distribution of the flow regimes depending on r_h introduced in Nezu et al. (1999) and used in Stocchino et al. (2011). As pointed out by Nezu et al. (1999) three different flow regimes can be identified depending on the value of r_h. For $r_h > 3$ the flow is defined as “Shallow”. In this case, intense velocity gradients occur at the transition between the main channel and the floodplains, leading to a strong shearing and a generation of vorticity associated with the flow depth jump Soldini et al. (2004). For values of $r_h < 2$, the flow is defined as “Deep”, characterized by a weaker shear in the transition region. The flow depth jump, in this case, is unable to greatly influence the free-surface flow. Finally, “Intermediate flows” are defined when $2 < r_h < 3$. In the framework of their analysis Stocchino et al. (2011) evaluated single and multiple particles statistics. Since a constant mean velocity causes the absolute dispersion to increase quadratically in time, and thus the diffusivity to increase linearly in time, their analysis was carried out removing a constant mean from the velocity field. In the case of compound channel flows, a mean motion does exist in the stream-wise direction and it is non-homogeneous over the cross-section. The mean stream-wise velocity assumes a bell-like distribution as shown in Stocchino and Brocchini (2010) and its shape depends strongly on the flow depth ratio r_h. As a result, for a 2D flow evolving in the plane the residual velocity reads as

$$\boldsymbol{u}'(x, y, t) = \boldsymbol{u}(x, y, t) - \boldsymbol{U}(x, y) \tag{23}$$

where $\boldsymbol{U}(x, y)$ indicates the velocity averaged over the duration of the single realization. This method is adequate to handle flows that are inhomogeneous, like in the present case or in oceanographic applications, while the classical results of Taylor were obtained assuming $\boldsymbol{U}(x, y) = 0$, i.e. for homogeneous flows. The analysis is then carried out upon such velocity field in agreement with Stocchino et al. (2011).

SLS and JC have been computed on the entire dataset. However, for the sake of clarity, we will discuss in details one run of each class, showing the recurrent features of every corresponding class.

Table 1
Main experimental parameters.

EXP Series	No. of runs	r_h (-)	Fr (-)	S (-)	$Re \times 10^4$ (-)
100	12	1.28 – 3.70	0.14 – 1.12	0.0064	2.8 – 14.2
200	13	1.68 – 4.16	0.60 – 0.82	0.0032	2.0 – 13.0
E0	10	1.82 – 3.69	0.87 – 1.13	0.0064	2.8 – 13.1
E00	9	1.77 – 3.69	0.44 – 0.57	0.0016	1.3 – 5.2
E00	9	1.82 – 4.42	0.73 – 0.99	0.0048	1.2 – 9.9

3.1. Assessment of two-dimensionality

In the framework of the present work, the fluid flow is considered two-dimensional. Indeed, the measurements presented in Stocchino and Brocchini (2010) and Stocchino et al. (2011) were taken on the free surface assuming that the flow is mainly two dimensional. This experimental approach based on the free surface velocity measurement is often used in many experimental works with primary focus on quasi-2D vortical structures (see Jirka, 2001; Nikora et al., 2007; Socolofksy and Jirka, 2004, among others). This approach is valid as long as the secondary flows can be considered negligible in the formation of the quasi-2D vortical structures with vertical axis of rotation and confined in a layer close to the bottom. However, in order to verify this hypothesis the Lagrangian divergence is here evaluated. In particular, Mathur et al. (2007) define Lagrangian divergence as:

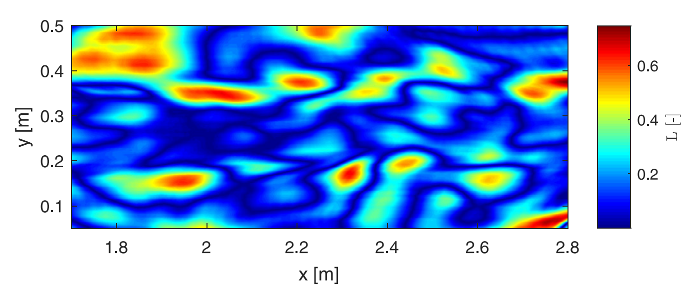

Fig. 5. Lagrangian divergence evaluated on a time interval of 1s for EXP 201.

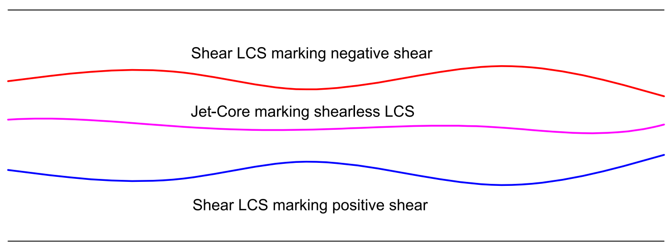

Fig. 6. Pictorial representation of the shear LCS of the compound channel, in red and blue. At the center of the main channel a JC is present, in magenta. (For interpretation of the references to colour in this figure legend, the reader is referred to the web version of this article.)

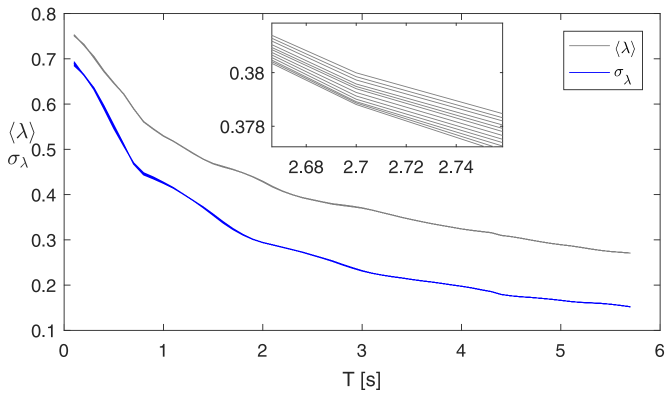

Fig. 7. FTLE average and standard deviation as a function of integration time for 12 different initial conditions. The close up helps in identifying the different curves.

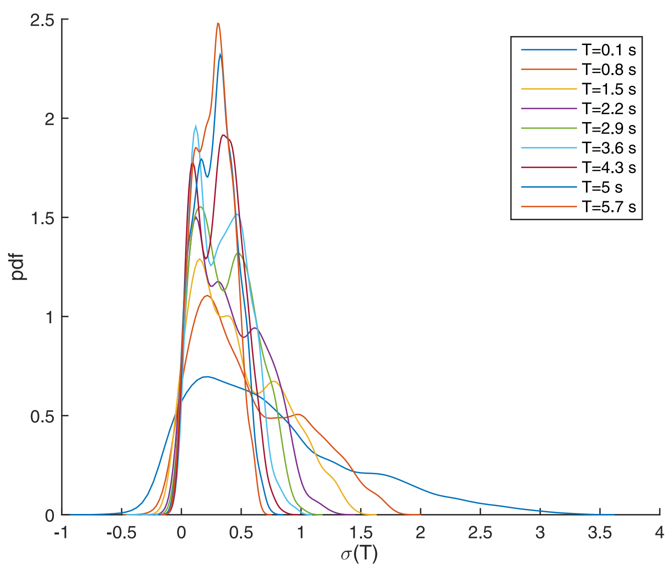

Fig. 8. Probability density function for FTLE fields.

$$L(\boldsymbol{x}) = \int_{t_0}^{t_1} [\nabla \cdot \boldsymbol{v}]_{\boldsymbol{\Phi}(t_0;t,\xi)} dt \tag{24}$$

where $\boldsymbol{v} = \boldsymbol{u}'$ in the present case. The Lagrangian divergence is computed along particle paths and should be zero for purely 2D flows. It represents the factor by which infinitesimal areas are magnified. Fig. 5 shows a typical snapshot of $L(\boldsymbol{x})$ for a shallow flow case. The Lagrangian divergence presents a quite flat distribution with the only exception of few peaks located at the transition region. The overall values are well below unity and much smaller than the ones found by Mathur et al. (2007) in a rotating water tank where the flow is considered manly two-dimensional. This measure is also employed by Wilson et al. (2013) in a turbulent boundary layer in order to quantify its two-dimensionality. They found a mean value of $\exp(L)$ close to 1.2 over their entire domain, arguing that stretching along one direction is balanced by convergence in another direction. Further considerations led them to accept the flow as two-dimensional.

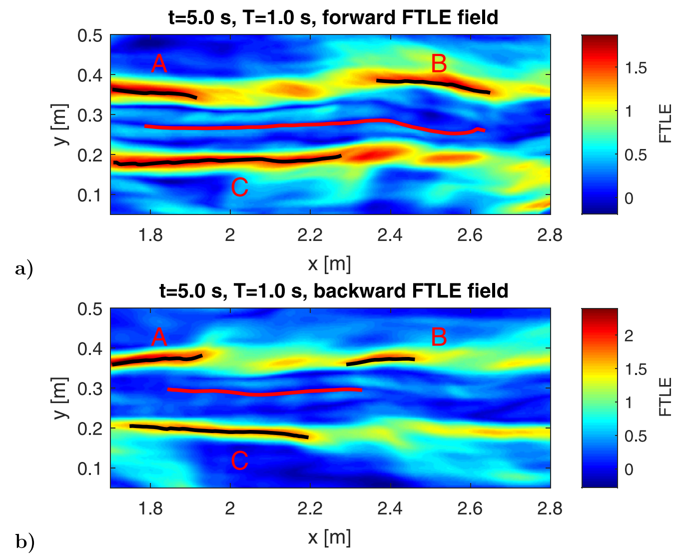

Fig. 9. Forward and backward FTLE ridges for EXP 201, shallow flow conditions. Letters identify predominant FTLE ridges. Trenches are marked in red. (For interpretation of the references to colour in this figure legend, the reader is referred to the web version of this article.)

Besides, divergence-free flows have FTLE fields non-negative (Arnold, 1992; Lipinski and Mohseni, 2010). Therefore, an indirect proof of the low three-dimensionality of the flow can be obtained inspecting FTLE fields. As showed in the following Sections negative FTLE values are very few. Therefore, the assumption of two-dimensionality can be fully accepted.

4. Results

Four experimental cases are reported in detail as prototypical examples of the respective flow conditions: shallow flows, intermediate flows and deep flows. In the case of intermediate flows, two regimes have been further investigated, namely flow in subcritical and supercritical conditions. The integration time is set to one second in order to let particle stay inside the computational domain. Furthermore, such an integration time has the same order of magnitude of the Lagrangian decorrelation time evaluated by Stocchino et al. (2011) on the same dataset.

It is worthy to recall the theoretical analysis reported in Haller and Beron-Vera (2012), where the authors studied a parallel shear flow as a benchmark case. In particular, the velocity field of the shear flow investigated takes the form

$$\dot{x} = u(y, t) \tag{25}$$

$$\dot{y} = v(y) \tag{26}$$

on a planar domain with non-vanishing and non-linear time-averaged shear $\left(a(y) = \int_{t_0}^{t} u(y, \tau) d\tau \neq 0 \text{ and } da(y)/dy \neq 0\right)$. One of the main conclusions of the work by Haller and Beron-Vera (2012) was that, in such a framework, any horizontal line is a shear LCS. Despite several important differences, it is possible to cast an analogy between the above flow and the compound channel flows here discussed. Indeed, although both velocity components are time dependent in the case of compound channels, the shear pattern heuristically conforms to the parallel shear flow described by Eqs. (25) and (26), since shear LCS do develop in the stream-wise direction and are advected in the same direction.

In particular, the expected pattern must be symmetric with respect to the axis of the channel because the residual velocity, Eq. (23), upon

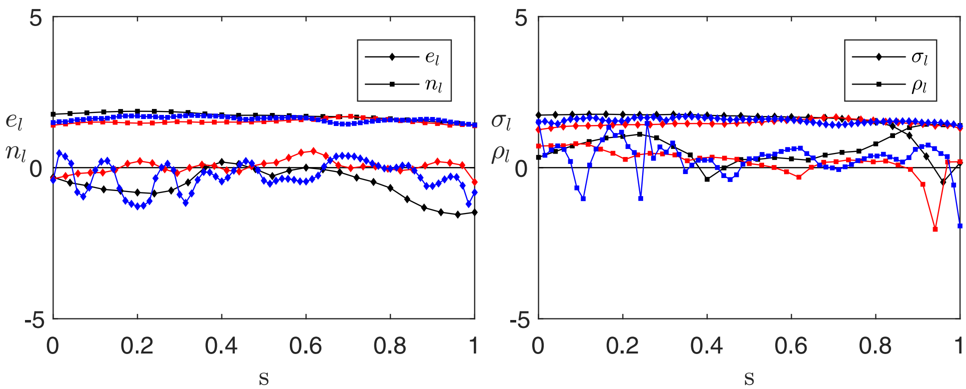

Fig. 10. Forward FTLE ridges normal and tangential advected unit vector magnitudes, e_l and n_l on the left, and hyperbolic repulsion and Lagrangian shear, σ_l and ρ_l on the right. Black, red and blue colors refer to ridges A, B and C of Panel a) of Fig. 9, respectively. (For interpretation of the references to colour in this figure legend, the reader is referred to the web version of this article.)

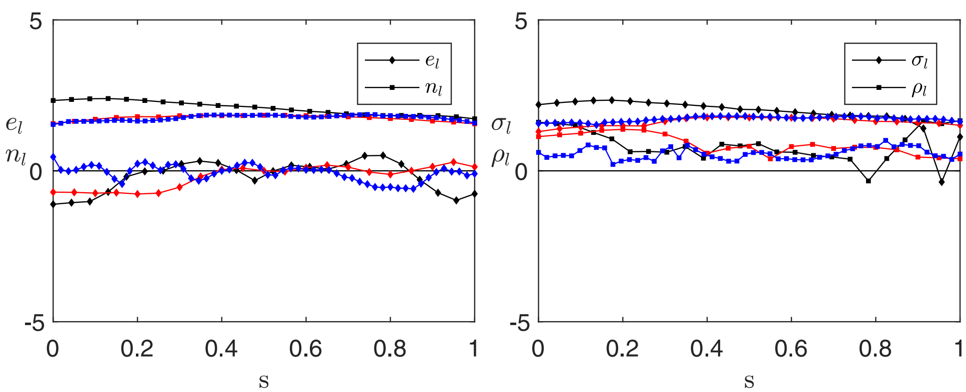

Fig. 11. Backward FTLE ridges normal and tangential advected unit vector magnitudes, e_l and n_l on the left, and hyperbolic repulsion and Lagrangian shear, σ_l and ρ_l on the right. Black, red and blue colors refer to ridges A, B and C of Panel b) of Fig. 9, respectively. (For interpretation of the references to colour in this figure legend, the reader is referred to the web version of this article.)

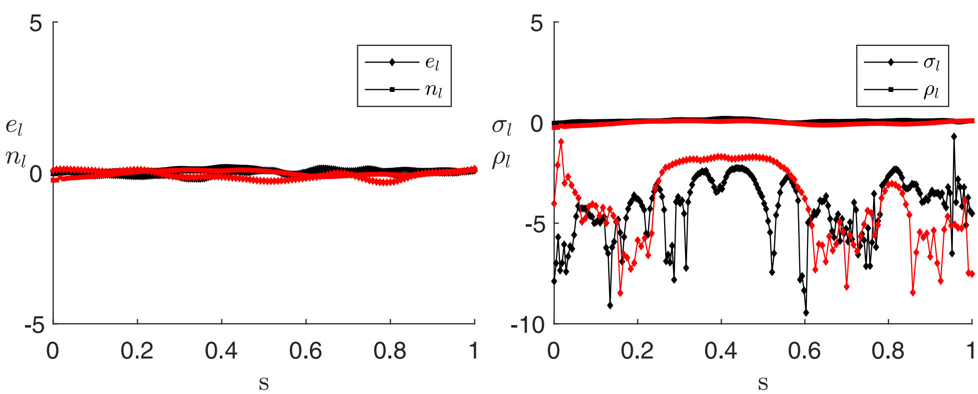

Fig. 12. Quantification of repelling and shear properties of JC. Panel a) shows n_l and e_l for forward and backward trenches of Fig. 9, in red and black respectively. Panel b) shows ρ_l and σ_l with the same color coding. (For interpretation of the references to colour in this figure legend, the reader is referred to the web version of this article.)

which Eq. (2) is solved determines a flow direction of the main channel reversed with respect to the floodplains. Fig. 6 shows a pictorial representation of shear LCS marking positive and negative shear, which can be detected in compound channels at the transition between the main channel and the floodplains. Indeed, the bottom region of the Figure shows positive shear whereas the top region negative shear, defined in agreement with the convention adopted for Eq. (20).

A shearless structure is present along the axis of the main channel marking a JC. The main channel is characterized by low values of FTLE fields and trenches can be detected. This is the typical configuration resulting from a bell-shaped velocity profile.

In the following, we present the main results obtained starting from a general description of the behaviour of the FTLE fields and then go forward with a detailed description of the Lagrangian structures depending on the flow regime.

4.1. General behaviour of FTLE fields

Coherent patterns are firstly detected through FTLE fields and they are found to behave in agreement with Eqs. (10) and (11). By choosing 12 different initial conditions and evaluating FTLE fields with integration times varying from 0.1 to 5.7 s, we can obtain the results plotted in Fig. 7. This Figure shows two bundles of 12 curves representing the average and the standard deviation of the values of FTLE fields as a function of the integration time. Note that the different curves are so closed to each other that can be hardly identified separately. The trends of both quantities, average and standard deviation, are in agreement with the expected theoretical results for ergodic systems, showing a monotonic decay in time as predicted by Abraham and Bowen (2002).

Moreover, the probability density function (pdf) of the FTLE are expected to behave accordingly. In particular, as the integration time increases the pdf tends to a Dirac delta centered at the limit FTLE value, see Fig. 8. Owing to the two-dimensionality of the flow at hand, it is reasonable to expect that FTLE values are mainly positive, leading to positively skewed pdfs.

4.2. Shear and shearless structures in shallow conditions

Experiment 201 is considered as a prototypical case of shallow conditions since it was carried out with a ratio $r_h = 4.16$. Note that the

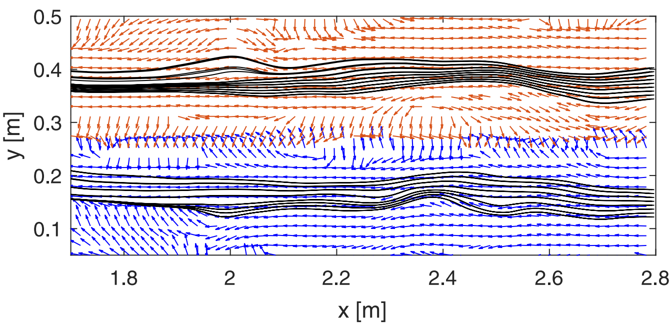

Fig. 13. Positive, in blue, and negative shear vector field, in red. Positive and negative shear LCS are superimposed on the respective fields. (For interpretation of the references to colour in this figure legend, the reader is referred to the web version of this article.)

flow for this case is in subcritical regime ($F_r = 0.60$). Fig. 9 shows typical Lagrangian patterns of shallow flow conditions. Panel a) and b) depict a snapshot of the forward and backward FTLE fields evaluated at $t = 5.0$ s, respectively. Both forward and backward fields show structures at the transition from the main channel to the lateral floodplains. Upon each field, three main structures depicted in black are identified and their ridges isolated. At the center of the main channel trenches are identified and depicted in red. In order to prove the predominant shear character of ridges, the magnitude of the advected unit normal and tangential vectors are computed taking advantage of Eqs. (14) and (15). Besides, repulsion and Lagrangian shear are evaluated applying Eqs. (16) and (17). Figs. 10 and 11 show such quantities as a function of the curvilinear coordinated s along forward and backward ridges, respectively.

In all cases the growth of the normal vectors is greater than the growth of the tangential vectors, i.e. n_l is greater then e_l. The growth of the normal vector $\boldsymbol{n_0}$ is predominantly due to Lagrangian shear, since σ_l is greater than ρ_l along each ridge for almost their entire length. Ridge C belonging to the forward field of Fig. 9, panel a), shows some noisy signal in the hyperbolic repulsion, depicted in Fig. 10. This behaviour is all but surprising since it is encountered even from dataset resulting from numerical simulations (Allshouse and Peacock, 2015b). These quantitative results suggest that material elements initially aligned along FTLE ridges will tend to move consistently without significant elongations. On the contrary, material elements initially perpendicular to the ridges will stretch because of shear.

Trenches of FTLE fields are identified at the center of the main channel where low FTLE values appear. These trenches behave as JC showing absence of shear. Panel a) of Fig. 12 shows that n_l and e_l are almost zero along the entire length of both JC evaluated from forward and backward fields. This means that along JC unit normal and tangential vectors are not significantly deformed. Panel b) show that ρ_l is

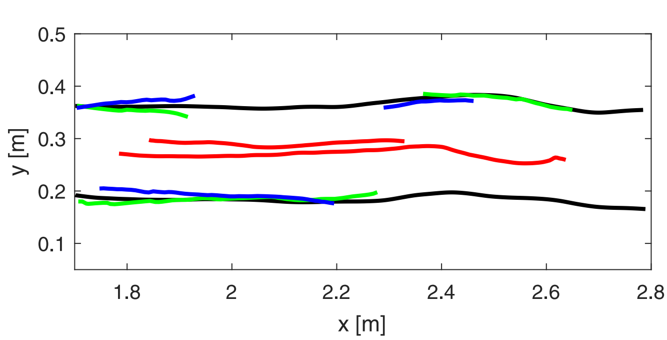

Fig. 14. Predominant positive and negative shearlines, in black, superimposed on forward FTLE field, EXP 201. Forward FTLE ridges, in green, and backward in blue. JC resulting from forward and backward FTLE fields are depicted in red. (For interpretation of the references to colour in this figure legend, the reader is referred to the web version of this article.)

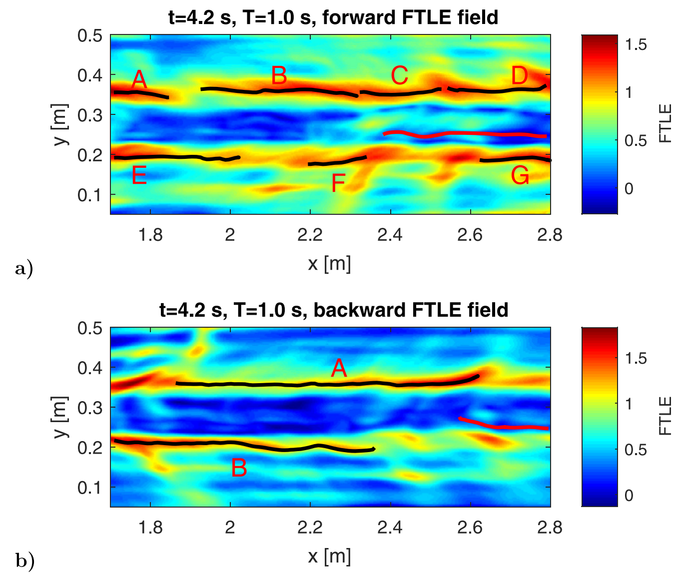

Fig. 15. Forward and backward FTLE ridges for EXP 207, intermediate flow conditions, subcritical case. Letters identify predominant FTLE ridges. Trenches are marked in red. (For interpretation of the references to colour in this figure legend, the reader is referred to the web version of this article.)

almost zero whereas σ_l is very small. This reflects the fact that unit normal vectors do not deform and their projection along the tangential direction to the ridge is negligible.

FTLE ridges are nicely in agreement with shearlines. Fig. 13 shows positive shear vector field (in the lower part of the domain, in blue) and negative shear vector field (in the upper part of the domain, in red). Shear vector fields and shearlines are computed through Eqs. (19) and (20), respectively. The corresponding positive and negative shearlines are superimposed on the corresponding areas. This particular pattern is due to the symmetry of the problem. Clockwise shear in the lower part of the domain is reflected in counterclockwise shear in the upper part of the domain (see for comparison Fig. 6). Fig. 14 shows the predominant shear LCS (in black) that minimize the geodesic deviation. Forward ridges of Fig. 9 are plotted in green and backward ridges in blue. They are not perfectly aligned with shear LCS since the eigenvectors associated with maximum eigenvalues differ from the shear vector field. However, their alignment is remarkable. JC are depicted in red and are located at the center of the main channel. They do not perfectly superimpose. Increasing the integration time should lead to a better superposition. However, this leads to an accumulation of particles to the boundaries resulting in a splintering of the ridges. As a result, the integration time is kept to one second.

4.3. Shear and shearless structures in intermediate conditions - subcritical case

Experiment 207 was carried out with a ratio $r_h = 2.26$ and it belongs to intermediate and subcritical conditions ($Fr = 0.73$). It is analyzed as a reference configuration for this type of flows. FTLE fields show in general a pattern comparable to shallow conditions even if high FTLE regions protrude towards lateral channels. Fig. 15 shows the FTLE field and represents the general configuration of interest for forward and backward fields. Seven predominant ridges are identified in forward time and two in backward time. Their behaviour is characterized with the same procedure followed in the previous Section. Analogously to the shallow case, Lagrangian shear is predominant to repulsion, as depicted in Figs. 16 and 17, classifying these ridges as SLS. Compared to the shallow case, higher values of FTLE are obtained in the floodplains. Such values could reach peaks comparable to those of the transition region, see panel a) of Fig. 15. At the center of the main channel trenches of FTLE fields are identified. Fig. 18 quantifies shear properties

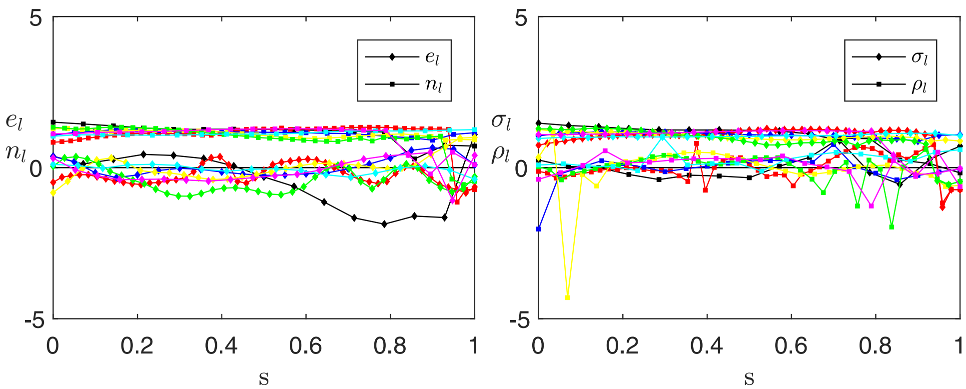

Fig. 16. Forward FTLE ridges normal and tangential advected unit vector magnitudes, e_l and n_l on the left, and hyperbolic repulsion and Lagrangian shear, σ_l and ρ_l on the right. Black, red, blue, yellow, green, cyan and magenta colors refer to ridges A, B, C, D, E and G of Panel a) of Fig. 15, respectively. (For interpretation of the references to colour in this figure legend, the reader is referred to the web version of this article.)

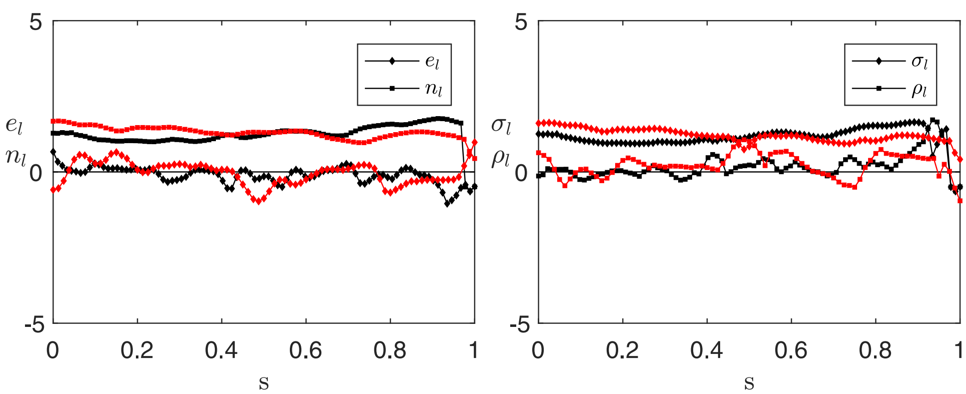

Fig. 17. Backward FTLE ridges normal and tangential advected unit vector magnitudes, e_l and n_l on the left, and hyperbolic repulsion and Lagrangian shear, σ_l and ρ_l on the right. Black and red colors refer to ridges A and B of Panel b) of Fig. 15, respectively. (For interpretation of the references to colour in this figure legend, the reader is referred to the web version of this article.)

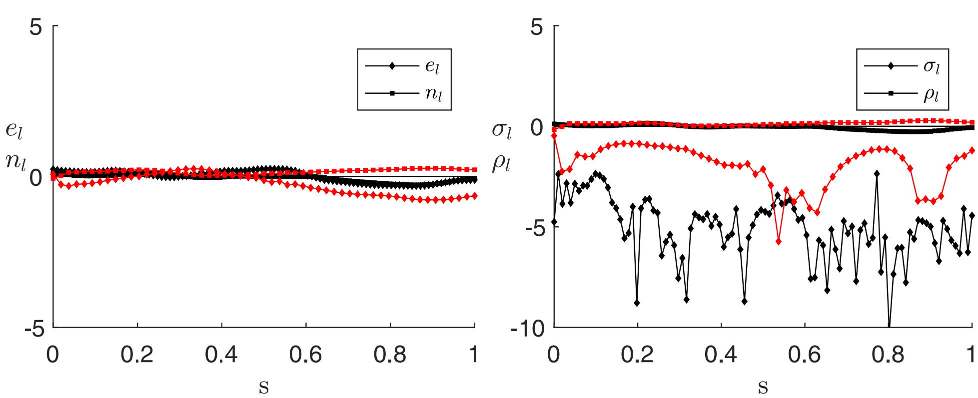

Fig. 18. Quantification of repelling and shear properties of JC. Panel a) shows n_l and e_l for forward and backward trenches of Fig. 15, in red and black respectively. Panel b) shows ρ_l and σ_l with the same color coding. (For interpretation of the references to colour in this figure legend, the reader is referred to the web version of this article.)

of such trenches and qualifies them as JC, showing results analogue to those of Experiment 201. However, the extension of the region where low FTLE values are present contracts.

Fig. 19 shows positive shear vector field (in the lower part of the domain, in blue) and negative shear vector field (in the upper part of the domain, in red) with a pattern analogous to the previous case. Fig. 20 shows the shear LCS that minimize the geodesic deviation alongside ridges and trenches. Shear LCS do align along longitudinal FTLE ridges. JC identified in both forward and backward fields superimpose much better than in the case of Experiment 201.

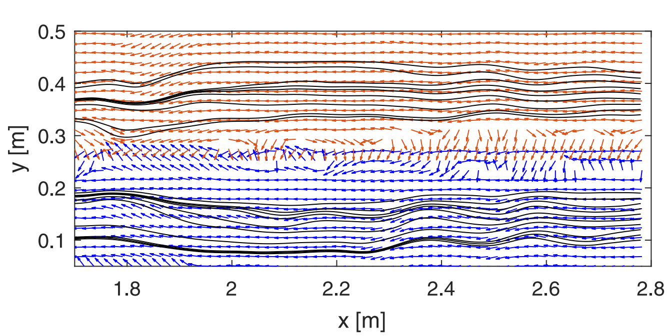

Fig. 19. Positive, in blue, and negative shear vector field, in red. Positive and negative shear LCS are superimposed on the respective fields. (For interpretation of the references to colour in this figure legend, the reader is referred to the web version of this article.)

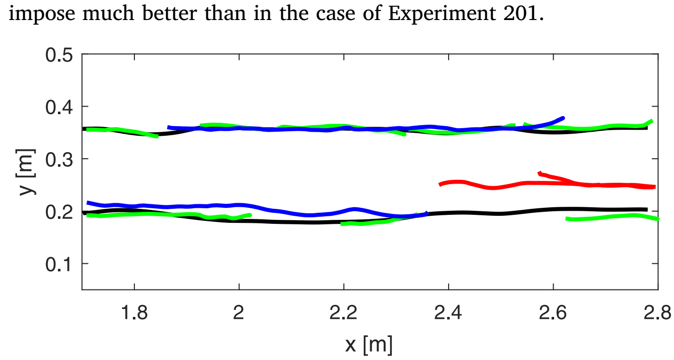

Fig. 20. Predominant positive and negative shearlines, in black, superimposed alongside with forward FTLE ridges, in green, and backward in blue. JC are depicted in red. (For interpretation of the references to colour in this figure legend, the reader is referred to the web version of this article.)

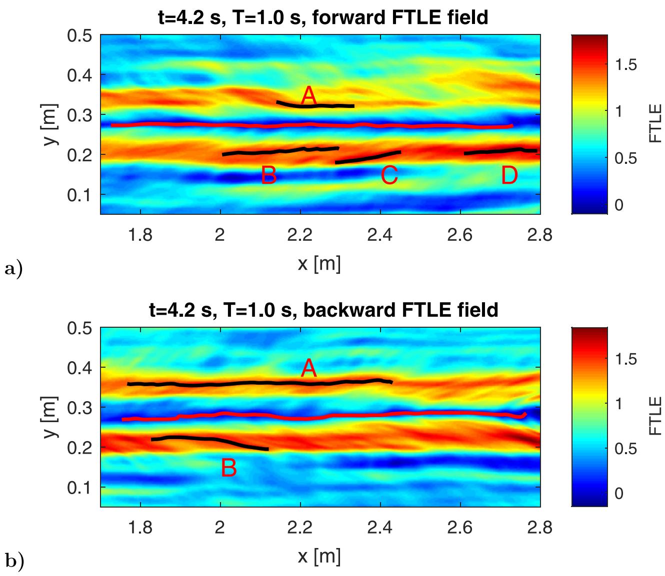

Fig. 21. Forward and backward FTLE ridges for EXP 105, intermediate flow conditions, supercritical case. Letters identify predominant FTLE ridges. Trenches are marked in red. (For interpretation of the references to colour in this figure legend, the reader is referred to the web version of this article.)

4.4. Shear and shearless structures in intermediate conditions - supercritical case

Experiment 105 was carried out with a ratio $r_h = 2.15$ belonging to intermediate and supercritical conditions ($Fr = 1.05$). FTLE fields show in general a pattern comparable to intermediate and subcritical conditions. Fig. 21 shows the FTLE field representing the general configuration of interest for forward and backward fields.

Four predominant ridges are identified in forward time and two in backward time. Higher FTLE values are located at the transition region. However, some ridges do not completely align along the stream-wise direction. In particular ridges C of panel a) and B of panel b) of Fig. 21 tend to align diagonally with respect to the stream-wise direction. As a result, for these specific ridges, Lagrangian shear is not always predominant over hyperbolic repulsion. Figs. 22 and 23 show that the magnitude of the advected normal is always greater than the magnitude of the advected tangential vector for all the ridges. Such predominance is due to Lagrangian shear except for the ridges with diagonal alignment. Therefore, we do not classify these ridges as SLS since they show for a non-negligible length a hyperbolic behaviour. Very well defined trenches are detected at the center of the main channel. Fig. 24 shows the shear properties of these trenches that qualify as JC with negligible shear.

Fig. 25 shows positive shear vector field (in the lower part of the domain, in blue) and negative shear vector field (in the upper part of the domain, in red) with a pattern analogous to the previous case. Fig. 26 shows the shear LCS that minimize the geodesic deviation. These shear LCS align with ridges of FTLE fields except for ridges C of panel a) and B of panel b) of Fig. 21. This explains why hyperbolic repulsion is predominant over Lagrangian shear along some portions of these ridges. On the contrary, JC are very well superimposed.

4.5. Shear and shearless structures in deep conditions

Experiment 213 was carried out with a ratio $r_h = 1.68$ and in subcritical conditions ($Fr = 0.82$). It is analysed as a reference configuration for deep flow conditions. FTLE fields show in general a pattern with the absence of persistent structures. Fig. 27 shows the FTLE field representing the general configuration of interest for forward and backward fields. In deep conditions the FTLE field is less readable and regions with high FTLE values protrude towards the inner of the main

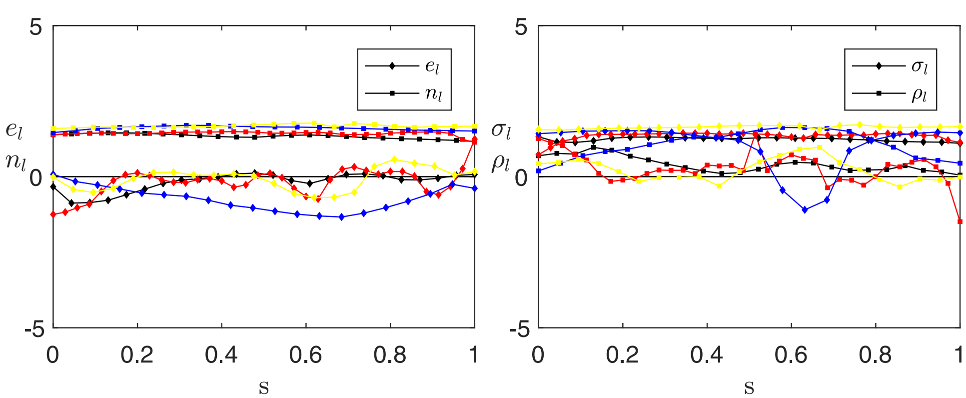

Fig. 22. Forward FTLE ridges normal and tangential advected unit vector magnitudes, e_l and n_l on the left, and hyperbolic repulsion and Lagrangian shear, σ_l and ρ_l on the right. Black, red, blue and yellow colors refer to ridges A, B, C and D of Panel a) of Fig. 21, respectively. Hyperbolic repulsion of ridge C is comparable and even predominant over Lagrangian shear. (For interpretation of the references to colour in this figure legend, the reader is referred to the web version of this article.)

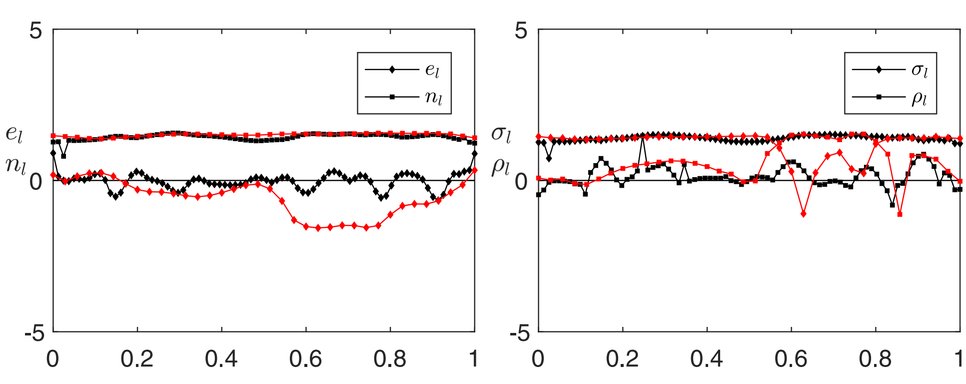

Fig. 23. Backward FTLE ridges normal and tangential advected unit vector magnitudes, e_l and n_l on the left, and hyperbolic repulsion and Lagrangian shear, σ_l and ρ_l on the right. Black and red colors refer to ridges A and B of Panel b) of Fig. 21, respectively. Hyperbolic repulsion of ridge B is predominant over Lagrangian shear along a significant portion of its length. (For interpretation of the references to colour in this figure legend, the reader is referred to the web version of this article.)

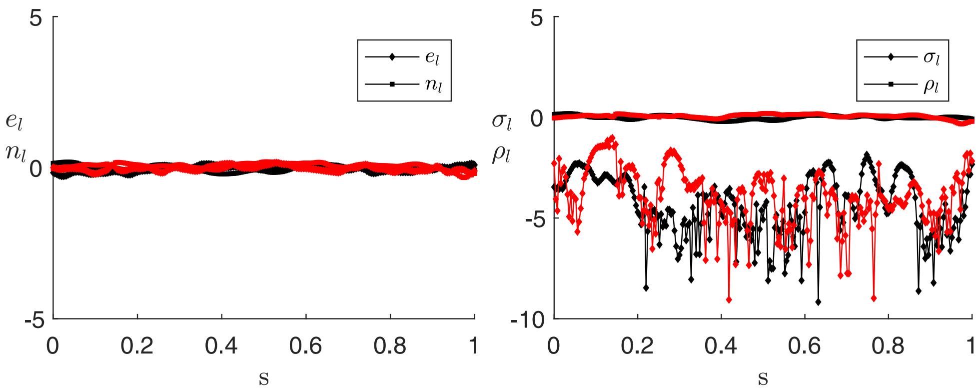

Fig. 24. Quantification of repelling and shear properties of JC. Panel a) shows n_l and e_l for forward and backward trenches of Fig. 21, in red and black respectively. Panel b) shows ρ_l and σ_l with the same color coding. (For interpretation of the references to colour in this figure legend, the reader is referred to the web version of this article.)

channel. Four predominant ridges are identified in forward time and two in backward time. Their behaviour is characterized with the same procedure followed in the previous Sections. Analogously to the previous cases, Lagrangian shear is predominant to repulsion, as depicted in Fig. 28, for ridges that are mainly longitudinal, i.e A and C of the forward field (panel a) of Fig. 27). Transverse ridges, B and D, show, on the contrary, comparable Lagrangian shear and repulsion strength and, consequently, cannot be classified as a SLS. Such a behaviour, showed in Fig. 29, characterizes even ridge B belonging to the backward field (panel b) of Fig. 27). Trenches are located at the center of the main channel. However, the width of the low FTLE region has shrunk significantly compared to the previous cases. As a result, trenches tend to be interrupted by higher values of FTLE. Fig. 30 quantifies the shear properties of these trenches that can be consequently classified as JC.

Fig. 31 shows positive shear vector field (in the lower part of the domain, in blue) and negative shear vector field (in the upper part of the domain, in red) with a pattern analogous to the previous case. Fig. 32 shows the shear LCS that minimize the geodesic deviation. These shear LCS do align along longitudinal FTLE ridges. JC do superimpose as expected.

As a general comment of such a flow condition it is possible to argue a strong independence of the surface flow from the depth jump. Indeed, transition region from the main channel to the floodplains is not clearly marked by high FTLE regions as in the previous cases. Furthermore, the presence of JC is not continuous along the stream-wise direction.

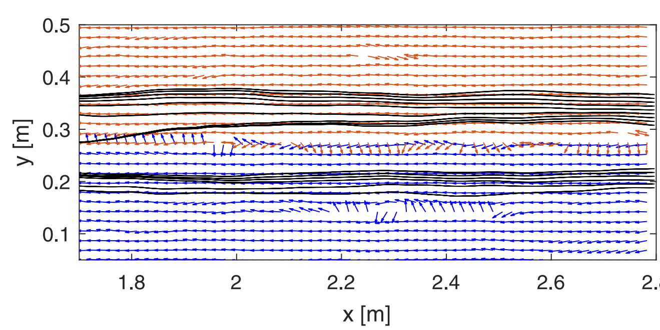

Fig. 25. Positive, in blue, and negative shear vector field, in red. Positive and negative shear LCS are superimposed on the respective fields. (For interpretation of the references to colour in this figure legend, the reader is referred to the web version of this article.)

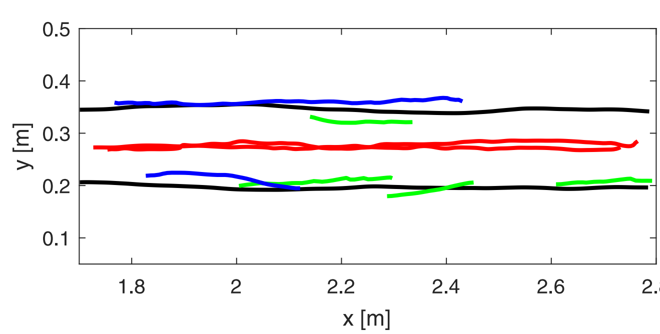

Fig. 26. Predominant positive and negative shearlines, forward FTLE ridges in green, backward in blue and JC in red. (For interpretation of the references to colour in this figure legend, the reader is referred to the web version of this article.)

5. Discussion and concluding remarks

This work aims to detect Shear and Shearless Lagrangian Coherent Structures in compound channels. Finite-Time Lyapunov Exponent fields are calculated on the basis of Eulerian velocity fields measured via PIV (Stocchino et al., 2011; Stocchino and Brocchini, 2010) and they unveil the most active regions of the fluid flow from a kinematic point of view. From a methodological perspective, ridges and trenches of FTLE fields are obtained combining the best methods found in literature: algorithm proposed by Mathur et al. (2007), Hermite interpolation by Haller (2011) (recovered in a simplified version from Rovenski (2010) owing to a predominant linearity of ridges and trenches along the stream-wise direction), refinement process proposed by Allshouse and Peacock (2015b). Note that the Eulerian velocity fields were collected during an experimental campaign whereas most applications concern analytical or numerical models. This reinforce the idea that this Lagrangian measure is a robust tool that can be applied to

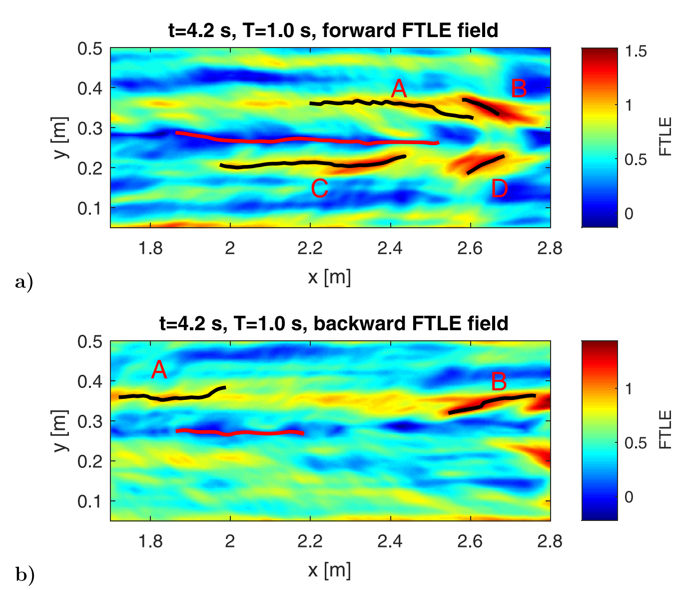

Fig. 27. Forward and backward FTLE ridges for EXP 213, deep flow conditions. Letters identify predominant FTLE ridges. Trenches are marked in red. (For interpretation of the references to colour in this figure legend, the reader is referred to the web version of this article.)

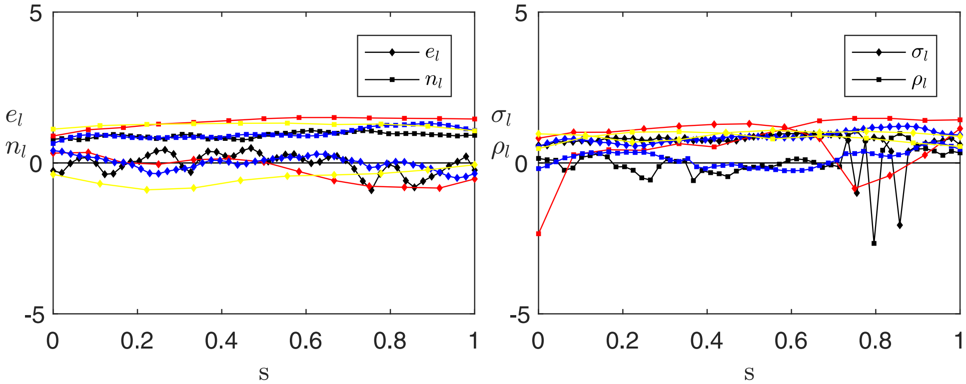

Fig. 28. Forward FTLE ridges normal and tangential advected unit vector magnitudes, e_l and n_l on the left, and hyperbolic repulsion and Lagrangian shear, σ_l and ρ_l on the right. Black, red, blue and yellow colors refer to ridges A, B, C and D of Panel (a) of Fig. 27, respectively. Ridges B and D show hyperbolic repulsion and Lagrangian shear of comparable strength. (For interpretation of the references to colour in this figure legend, the reader is referred to the web version of this article.)

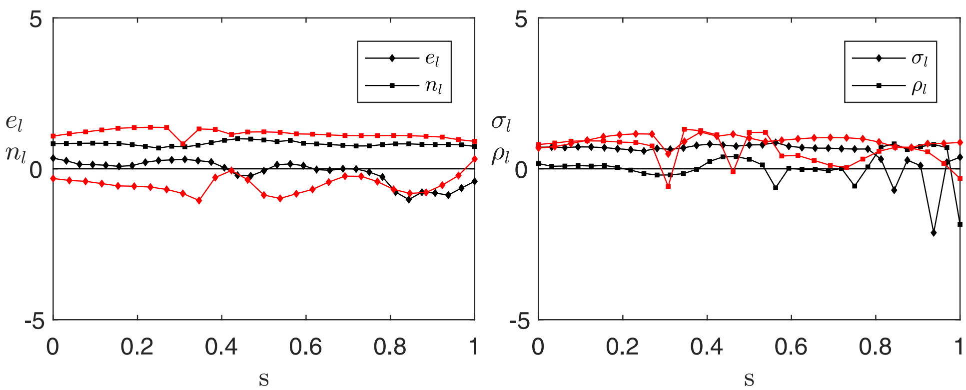

Fig. 29. Backward FTLE ridges normal and tangential advected unit vector magnitudes, e_l and n_l on the left, and hyperbolic repulsion and Lagrangian shear, σ_l and ρ_l on the right. Black and red colors refer to ridges A and B of Panel (b) of Fig. 27, respectively. Ridge B shows hyperbolic repulsion and Lagrangian shear of comparable strength. (For interpretation of the references to colour in this figure legend, the reader is referred to the web version of this article.)

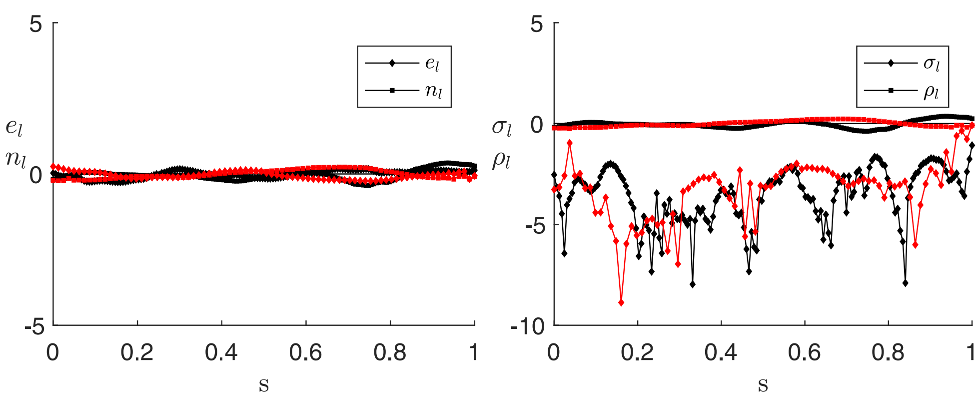

Fig. 30. Quantification of repelling and shear properties of JC. Panel a) shows n_l and e_l for forward and backward trenches of Fig. 27, in red and black respectively. Panel (b) shows ρ_l and σ_l with the same color coding. (For interpretation of the references to colour in this figure legend, the reader is referred to the web version of this article.)

realistic and complex flow fields.

The main parameters controlling the flow under investigation are the depth ratio r_h, i.e. the ratio between the depth of the main channel and the depth of the floodplains, and the Froude number. The first parameter defines the shallowness of the flow whereas the second the critical conditions.

The results suggest a strong influence of the depth ratio on the establishment of persistent Lagrangian patterns, whereas the Froude number do not seem to be an important controlling parameter. However, our dataset does not present supercritical flows for the shallow conditions and the highest Froude number is 1.07 for the intermediate conditions. Therefore, the relevance of our results mainly concerns the influence of the depth ratio.

In shallow flow conditions, FTLE fields show active regions at the transition from the main channel to the lateral floodplains marked by high FTLE values. Regions of small FTLE values at the center of the main channel are also present. The former are associated with ridges whereas the latter with trenches. Ridges mark Shear Lagrangian Structures that maximize Lagrangian shear and trenches Shearless Lagrangian Structures that behave as Jet-Cores.

Such a configuration is kept even in intermediate conditions. However, it is possible to observe that FTLE ridges protrude more in the

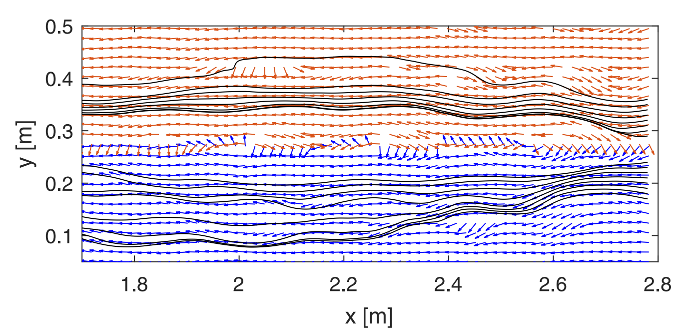

Fig. 31. Positive, in blue, and negative shear vector field, in red. Positive and negative shear LCS are superimposed on the respective fields. (For interpretation of the references to colour in this figure legend, the reader is referred to the web version of this article.)

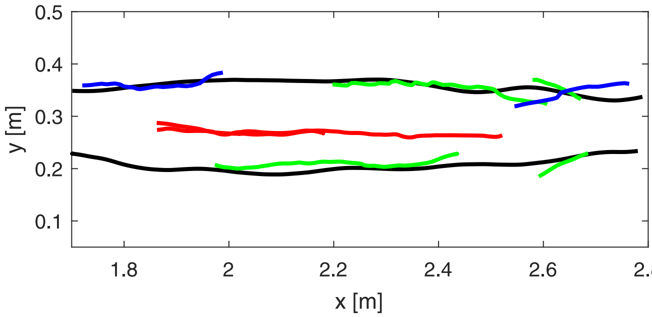

Fig. 32. Predominant positive and negative shearlines, in black, superimposed on forward FTLE field, EXP 213. Forward FTLE ridges in green, backward in blue and JC in red. (For interpretation of the references to colour in this figure legend, the reader is referred to the web version of this article.)

floodplains. The analysis performed on the resulting ridges in order to assess whether hyperbolic repulsion or Lagrangian shear are predominant suggests that ridges aligned along the stream-wise direction show predominance of Lagrangian shear over hyperbolic repulsion. On the contrary, ridges that are aligned diagonally with respect to the stream-wise direction show portions of their length where hyperbolic repulsion is predominant over Lagrangian shear.

The clear separation between the main channel and the floodplains shades by decreasing the flow depth ratio and reaching deep flow conditions. As a result, the presence of Shear and Shearless Lagrangian Structures detected from FTLE fields is less readable. It is still possible to recover some features but their persistence is less evident.

The peculiar pattern of shallow and intermediate conditions strongly influences transport as Fig. 33 exemplifies. Green dots represent tracers advected by the flow. Panels (a), (c), (e) and (g) represent initial conditions of particles superimposed on forward FTLE fields. Panels (b), (d), (f) and (h) represent final conditions resulting from the advection process superimposed on corresponding forward FTLE fields. Note that, forward FTLE fields are usually associated with repelling structures. However, a negligible hyperbolic repulsion was detected for ridges aligned along the stream-wise direction in the previous paragraphs. Panels (a)–(f) refer to shallow and intermediate conditions. These clearly show the shear character of ridges at the transition region due to the fact that the initial distance between particles is not kept constant by the advection process. By decreasing r_h the shear character persists but with less strength. Jet-Cores at the centre of the main channel preserve the initial spacing between the particles. Panels (g) and (h) refer to deep conditions and they show that the shear strength tends to be lost.

This analysis gives an integrated point of view over a finite time interval of the previous work carried out by Stocchino and Brocchini (2010) and Stocchino et al. (2011). The influence of the Eulerian macrovortices that develop mainly in shallow conditions (cf. Fig. 4 of Stocchino et al., 2011) can be directly observed in the meandering pattern that particles show in such a flow (see panel b) of Fig. 33. However, Eulerian and Lagrangian diagnostics are conceptually different (Haller, 2015) since the former refer to an instantaneous time instance whereas the latter to a finite time interval. Therefore, a direct

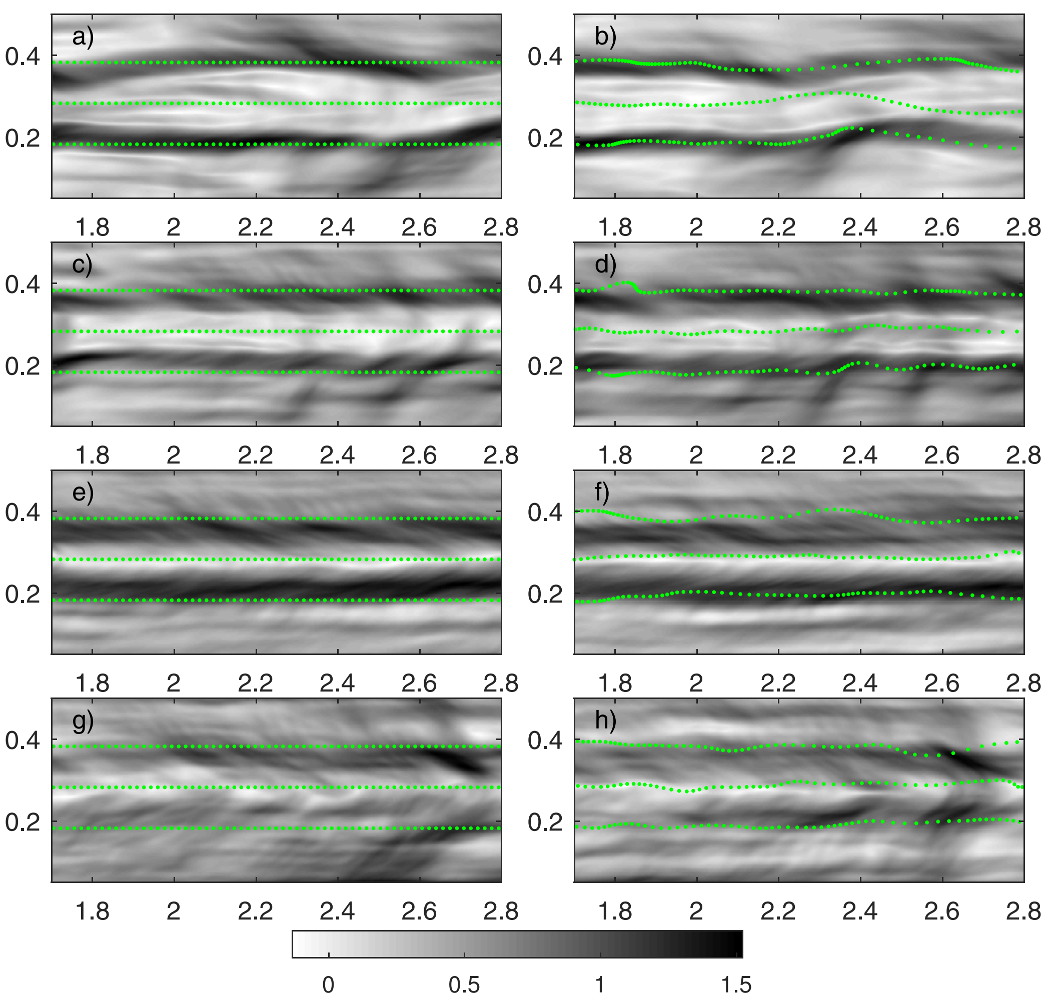

Fig. 33. Advection of particles (green dots) superimposed on corresponding forward FTLE fields (tones of grey). Left panels show initial conditions, right panels final conditions. Panel (a) and (b) refer to shallow conditions (EXP. 201). Panels (c)–(f) to intermediate conditions (EXP. 207 and EXP. 105, respectively). Panels (g) and (h) refer to deep conditions (EXP. 213). (For interpretation of the references to colour in this figure legend, the reader is referred to the web version of this article.)

matching is impossible to reach.

Ridges of FTLE fields marking heuristic SLS conform to rigorous SLS calculated adopting the geodesic theory of transport barriers (Haller and Beron-Vera, 2012). Such SLS are aligned along the stream-wise direction with a symmetric pattern. Positive SLS are located in the bottom part of the domain and negative SLS are located in the upper part of the domain. However, SLS are always aligned along the stream-wise direction.

Decreasing r_h down to a value typical of deep flow conditions, SLS conform to shallow and intermediate conditions. However, the results should be considered jointly with the fact that FTLE fields are less significant and do not show strong persistent patterns. This fact reflects the different velocity profiles that are recovered in the different depth flow conditions along a cross-section. Fig. 2 of Stocchino and Brocchini (2010) shows that peak velocities in the main channel and in the floodplains are comparable at deep flow conditions.

Therefore, FTLE fields prove to be once again a valuable tool in order to assess the behaviour of a fluid flow giving an immediate understanding of the strength of the mixing pattern and the most active regions of the domain. However, these active areas need to be well characterized by the evaluation of the Lagrangian shear and the hyperbolic repulsion. To further understand the dynamics, SLS are detected in order to depict the shear pattern. The joint analysis of FTLE fields and SLS manage to unveil the mixing pattern thoroughly since the shortcomings of one measure are balanced by strengths of the other. Besides, the presence of JC at the center of the main channel impacts on tracer advection. These results are of evident importance in riverine and estuarine analysis since these structures mark regions where particles undergo different fates. For example, evaluation of concentration distributions employed in the advection-diffusion equation must carefully take into account the inhomogeneity resulting from SLS and JC. As a result, turbulent diffusivity can vary on the spatial domain (Besio et al., 2012) especially across regions delimited by SLS and JC. Natural streams or estuaries usually show several regions that adapt to the framework of this work. The presence of analogue structures is quite likely. Therefore, LCS should mark the natural boundaries along which diffusivities could dramatically change their magnitude. Further research is needed to clearly connect the Eulerian properties of the flow with its intrinsic Lagrangian features. Indeed, the compound channel geometry leads to the generation of Eulerian vortical structures, the appearance of which is strongly dependent on the flow depth ratio. The present results suggest that a similar relationship is found when Lagrangian Coherent Structures are studied. A link between the two frameworks based on the spectral properties of Eulerian velocity fields and FTLE fields would then be desirable.

Supplementary material

Supplementary material associated with this article can be found, in the online version, at 10.1016/j.advwatres.2018.01.006.

References

Abraham, E.R., Bowen, M.M., 2002. Chaotic stirring by a mesoscale surface ocean-flow. Chaos 12 (2), 373–381.
Allshouse, M.R., Peacock, T., 2015. Lagrangian based methods for coherent structures detection. Chaos 25 (9).
Allshouse, M.R., Peacock, T., 2015. Refining finite-time Lyapunov exponent ridges and the challenges of classifying them. Chaos 25 (8).
Aris, R., 1962. Vectors, Tensors, and the Basic Equations of Fluid Mechanics. Prentice-Hall, Englewood Cliffs, New Jersey.
Arnold, V.I., 1992. Ordinary Differential Equations. Springer.
Beron-Vera, F.J., Olascoaga, M.J., Brown, M.G., Koçak, H., Rypina, I.I., 2010. Invariant-tori-like Lagrangian coherent structures in geophysical flows. Chaos 20 (1), 017514.
Besio, G., Stocchino, A., Angiolani, S., Brocchini, M., 2012. Transversal and longitudinal mixing in compound channels. Water Resour. Res. 48 (12).
Eckmann, J.P., Ruelle, D., 1985. Ergodic theory of chaos and strange attractors. Rev. Mod. Phys. 57, 617–656.
Farazmand, M., Blazevski, D., Haller, G., 2014. Shearless transport barriers in unsteady two-dimensional flows and maps. Physica D 278, 44–57.
Farazmand, M., Haller, G., 2012. Computing Lagrangian coherent structures from their variational theory. Chaos 22 (1), 013128.
Green, M.A., Rowley, C.W., Haller, G., 2007. Detection of Lagrangian coherent structures in three-dimensional turbulence. J. Fluid Mech. 572 (-1), 111–120.
Hadjighasem, A., Farazmand, M., Haller, G., 2013. Detecting invariant manifolds, attractors, and generalized kam tori in aperiodically forced mechanical systems. Nonlinear Dyn. 73 (1), 689–704.
Haller, G., 2011. A variational theory of hyperbolic Lagrangian coherent structures. Physica D 240, 574–598. http://dx.doi.org/10.1016/j.physd.2010.11.010.
Haller, G., 2015. Lagrangian coherent structures. Ann. Rev. Fluid Mech. 47, 137–162.
Haller, G., Beron-Vera, F.J., 2012. Geodesic theory of transport barriers in two-dimensional flows. Physica D 241 (20), 1680–1702.
Haller, G., Yuan, G., 2000. Lagrangian coherent structures and mixing in two-dimensional turbulence. Physica D 147 (3), 352–370.
Jirka, G., 2001. Large scale flow structures and mixing processes in shallow flows. J. Hydraul Res. 39, 567–573.
Lapeyre, G., 2002. Characterization of finite-time Lyapunov exponents and vectors in two-dimensional turbulence. Chaos 12 (3), 688–698.
Lipinski, D., Mohseni, K., 2010. A ridge tracking algorithm and error estimate for efficient computation of lagrangian coherent structures. Chaos 20 (1), 017504.
Mathur, M., Haller, G., Peacock, T., Ruppert-Felsot, J.E., Swinney, H.L., 2007. Uncovering the lagrangian skeleton of turbulence. Phys. Rev. Lett. 98 (14), 144502.
Nezu, I., Onitsuka, K., Iketani, K., 1999. Coherent Horizontal Vortices in Compound Open Channel Flows. In: Singh, V.P., Seo, I.W., Sonu, J.H. (Eds.), Hydraulic Modeling. Water Resources Pub., Colorado, USA, pp. 17–32.
Nikora, V., Nokes, R., Veale, W., Davidson, M., Jirka, G., 2007. Large-scale turbulent structure of uniform shallow free-surface flows. Environ. Fluid Mech. 7, 159–172.
Onu, K., Huhn, F., Haller, G., 2015. LCS tool: a computational platform for lagrangian coherent structures. J. Comput. Sci. 7, 26–36.
Peikert, R., Gnther, D., Weinkauf, T., 2013. Comment on second derivative ridges are straight lines and the implications for computing lagrangian coherent structures. Physica D 242 (1), 65–66.
van Prooijen, B., Battjes, J., Uijttewaal, W., 2005. Momentum exchange in straight uniform compound channel flow. J. Hydraul. Res. 131 (3), 175–183.
Rovenski, V., 2010. Modeling of Curves and Surfaces with MATLAB, 1st. Springer Publishing Company, Incorporated.
Rowiński, P., Radecki-Pawlik, A., 2015. Rivers–Physical, Fluvial and Environmental Processes. Springer.
Rypina, I.I., Brown, M.G., Beron-Vera, F.J., Koçak, H., Olascoaga, M.J., Udovydchenkov, I.A., 2007. Robust transport barriers resulting from strong kolmogorov-arnold-moser stability. Phys. Rev. Lett. 98, 104102.
Samelson, R.M., 1992. Fluid exchange across a meandering jet. J. Phys. Oceanogr. 22 (4), 431–444.
Shadden, S.C., Lekien, F., Marsden, J.E., 2005. Definition and properties of lagrangian coherent structures from finite-time lyapunov exponents in two-dimensional aperiodic flows. Physica D 212, 271–304.
Socolofksy, S., Jirka, G., 2004. Large-scale flow structures and stability in shallow flows. J. Environ. Eng.Sci. 3, 451–462.
Soldini, L., Piattella, A., Brocchini, M., Mancinelli, A., Bernetti, R., 2004. Macrovortices-induced horizontal mixing in compound channels. Ocean Dyn. 54, 333–339.
Stocchino, A., Besio, G., Angiolani, S., Brocchini, M., 2011. Lagrangian mixing in straight compound channel. J. Fluid Mech. 675, 168–198.
Stocchino, A., Brocchini, M., 2010. Horizontal mixing of quasi-uniform straight compound channel flows. J. Fluid Mech. 643, 425–435.
Tang, X., Boozer, A., 1996. Finite time Lyapunov exponent and advection-diffusion equation. Physica D 95 (3), 283–305.
Thiffeault, J.-L., Boozer, A.H., 2001. Geometrical constraints on finite-time Lyapunov exponents in two and three dimensions. Chaos 11 (1), 16–28.
Wilson, Z.D., Tutkun, M., Cal, R.B., 2013. Identification of lagrangian coherent structures in a turbulent boundary layer. J. Fluid Mech. 728, 396–416.